arXiv:1605.07011v1 [physics.optics] 23 May 2016

Infrared refractive index dispersion of PMMA spheres from synchrotron extinction spectra

R. Blümel[1], M. Bağcıoğlu[2], R. Lukacs[2], and A. Kohler[2]

[1]*Department of Physics, Wesleyan University, Middletown, Connecticut 06459-0155 and*

[2]*Department of Mathematical Sciences and Technology, Faculty of Environmental Science and Technology, Norwegian University of Life Sciences, 1432 Ås, Norway*

(Dated: May 24, 2016)

Abstract

We performed high-resolution Fourier-transform infrared (FTIR) spectroscopy of a polymethyl methacrylate (PMMA) sphere of unknown size in the Mie scattering region. Apart from a slow, oscillatory structure (wiggles), which is due to an interference effect, the measured FTIR extinction spectrum exhibits a ripple structure, which is due to electromagnetic resonances. We fully characterize the underlying electromagnetic mode structure of the spectrum by assigning two mode numbers to each of the ripples in the measured spectrum. We show that analyzing the ripple structure in the spectrum in the wavenumber region from about $3000\,\mathrm{cm}^{-1}$ to $8000\,\mathrm{cm}^{-1}$ allows us to both determine the unknown radius of the sphere and the PMMA index of refraction, which shows a strong frequency dependence in this near-infrared spectral region. While in this paper we focus on examining a PMMA sphere as an example, our method of determining the refractive index and its dispersion from synchrotron infrared extinction spectra is generally applicable for the determination of the index of refraction of any transparent substance that can be shaped into micron-sized spheres.

PACS numbers: 87.64.km, 78.30.Jm, 42.25.Fx, 78.20.Ci, 87.64.Cc

I. INTRODUCTION

Although seemingly innocuous and analytically solvable within the theory of classical electromagnetism [1], the scattering of light from dielectric spheres ("Mie scattering" [2–4]) exhibits a multitude of interesting facets. For instance, it was not until the advent of modern digital computers (in this case the IBM 701, which became available in the early 1950s [5]) that the fully developed fine structure of the scattering cross section emerged [6]. Subsequently, this characteristic "ripple structure" [4] gave rise to a lively debate on the physical origin of the ripples [4, 7, 8] and led to some important applications, for instance the spectroscopy of ripples with the help of laser levitation [9, 10]. Even today, Mie scattering is important for applications ranging from light scattering of particles in the atmosphere [11] and colloidal solutions [2, 12] to its use as a reference system for infrared spectroscopy on single biological cells [13, 14]. It is the latter application that we have in mind when, in this paper, we study Mie scattering at PMMA spheres. While Fourier-transform infrared (FTIR) spectroscopy of PMMA spheres has been carried out in the wavenumber region up to $4000\,\mathrm{cm}^{-1}$ [13–15], one of the main points of this paper is to extend these measurements up to $8000\,\mathrm{cm}^{-1}$, where the ripple patterns start to be fully developed. This serves as a test case for the resolving power of FTIR spectroscopy for applications to non-spherical systems, such as biological cells [13, 16, 17]. We also present an algorithm that allows us to extract the radius and the index of refraction of micron-sized PMMA spheres from the ripple structure of measured FTIR spectra. This extends our knowledge of the PMMA index of refraction into the near-infrared region from $3000\,\mathrm{cm}^{-1}$ to $8000\,\mathrm{cm}^{-1}$, where literature data, to our knowledge, are absent. It also allows us to test and challenge extrapolation formulae for the index of refraction in this range of wavenumbers [18–21]. In general, we find that FTIR spectroscopy of PMMA spheres is an excellent technique to establish the limits of FTIR spectroscopy, in particular as far as resolution is concerned. It may be used for calibration of the FTIR equipment before spectra of biological samples are taken. From the theoretical point of view our experimental extinction spectra of synchrotron radiation on PMMA microspheres test the Mie theory of scattering on dielectric spheres. We accomplish this by classifying each ripple in the extinction curve of PMMA micro spheres with electromagnetic mode numbers that uniquely characterize the specific nature and physical origin of each individual ripple in the spectrum. Our methods may be applied to high-resolution

FTIR spectroscopy of micro-spheres of any transparent biological or inanimate material. In particular, we propose to use high-resolution FTIR spectroscopy in conjunction with our methods as a new spectroscopic tool for the determination of the index of refraction of transparent materials in the near- to far-infrared spectral regime, where FTIR spectroscopy is conventionally performed.

II. THEORY

To set the stage for the analysis of our synchrotron FTIR spectra, we present in this section some background material on the scattering of infrared radiation from non-absorbing dielectric spheres of radius R, geometric cross section $g = \pi R^2$, real refractive index n, and magnetic permeability $\mu = 1$. These assumptions are appropriate for the analysis of the experiments described in this paper in which we focus on scattering of infrared radiation at PMMA spheres ($\mu \approx 1$) in the spectral region from $3000\,\mathrm{cm}^{-1}$ to $8000\,\mathrm{cm}^{-1}$ in which there is very little absorption (n approximately real). In our FTIR synchrotron experiments, an infrared beam with intensity I_0 is incident on a dielectric sphere, where it may be scattered, absorbed, or transmitted into a detector with surface area $G > g$. The scattered intensity is denoted by I_{sca}, the absorbed intensity by I_{abs}, and the un-scattered intensity, directed strictly in forward direction, is denoted by I. The cross sections for scattering and absorption are denoted by σ_{sca} and σ_{abs}, respectively. We also define the extinction cross section $\sigma_{\mathrm{ext}} = \sigma_{\mathrm{sca}} + \sigma_{\mathrm{abs}}$ [4]. With the help of G and the cross sections we may compute the associated radiative powers $P_0 = I_0 G$, $P_{\mathrm{sca}} = I_0 \sigma_{\mathrm{sca}}$, $P_{\mathrm{abs}} = I_0 \sigma_{\mathrm{abs}}$, and $P = IG$. Conservation of power requires:

$$P_0 = P + P_{\mathrm{sca}} + P_{\mathrm{abs}}. \tag{1}$$

Therefore, from (1), we obtain

$$I_0 G = IG + I_0 \sigma_{\mathrm{sca}} + I_0 \sigma_{\mathrm{abs}} = IG + I_0 \sigma_{\mathrm{ext}}. \tag{2}$$

In our experiments we measure the *apparent absorbance*, defined as

$$A = -\log_{10}\left(\frac{I}{I_0}\right). \tag{3}$$

This quantity is called the apparent absorbance since it does not only include the intensity lost due to (chemical) absorption (i.e., the "true" absorption), but also the intensity lost via

scattering. Because of the finite area G of our detector, and because of its finite distance to the scatterer, apart from collecting the un-scattered intensity I, our detector also collects some scattered light. Therefore, the recorded intensity I is somewhat different from the un-scattered intensity in forward direction. However, since the scattered intensity reaching our detector is small, and since, in addition, we are mainly interested in the *structure* of the resulting extinction spectra, not absolute values of the extinction, we found this effect to be negligible.

Following [4], we define the extinction efficiency

$$Q_{\text{ext}} = \frac{\sigma_{\text{ext}}}{g}. \tag{4}$$

To convert the results of our absorbance measurements to Q_{ext}, we proceed as follows. From (3) we obtain

$$\left(\frac{I}{I_0}\right) = 10^{-A}. \tag{5}$$

Dividing (2) by $I_0 G$ and using (4) and (5), we obtain

$$1 = \frac{I}{I_0} + \frac{\sigma_{\text{ext}}}{G} = 10^{-A} + \frac{g}{G} Q_{\text{ext}}, \tag{6}$$

from which we obtain

$$Q_{\text{ext}} = \left(\frac{G}{g}\right)\left(1 - 10^{-A}\right). \tag{7}$$

For dielectric spheres the extinction efficiency Q_{ext} can be computed analytically. This was first accomplished by Mie in 1908 [2] and further developed by Debeye in 1909 [3]. In the modern literature the result is usually quoted either in the notation of van de Hulst [4] or Newton [22]. In the notation of van de Hulst we have

$$Q_{\text{ext}} = \frac{2}{x^2} \sum_{n=1}^{\infty} (2n+1) \Re(a_n + b_n), \tag{8}$$

where a_n and b_n denote the complex-valued Mie coefficients [4], $\Re$ denotes the real part,

$$x = kR = 2\pi R/\lambda = 2\pi R\tilde{\nu} \tag{9}$$

is the size parameter, λ is the vacuum wavelength, $\tilde{\nu} = 1/\lambda$ is the wavenumber, and $k = 2\pi/\lambda = 2\pi\tilde{\nu}$ is the angular wavenumber. In the notation of Newton [22] we have

$$Q_{\text{ext}} = \frac{1}{x^2} \sum_{J=1}^{\infty} (2J+1) \left(2 - \Re S_e^J - \Re S_m^J\right), \tag{10}$$

where S_e^J and S_m^J are the scattering matrix (S-matrix) elements for electric and magnetic multipole radiation of order 2^J, respectively. Explicitly, S_e^J and S_m^J are given by

$$S_e^J(x;n) = e^{i\pi J}\ \frac{n w_J^{(-)'}(x) u_J(nx) - w_J^{(-)}(x) u_J'(nx)}{n w_J^{(+)'}(x) u_J(nx) - w_J^{(+)}(x) u_J'(nx)} \tag{11}$$

and

$$S_m^J(x;n) = e^{i\pi J}\ \frac{w_J^{(-)'}(x) u_J(nx) - n w_J^{(-)}(x) u_J'(nx)}{w_J^{(+)'}(x) u_J(nx) - n w_J^{(+)}(x) u_J'(nx)}, \tag{12}$$

where $J \geq 1$ and $u_J(z)$ and $w_J^{(\pm)}(z)$ are defined with the help of the spherical Bessel functions $j_J(z)$ and $n_J(z)$ [22, 23] according to

$$\begin{aligned} u_J(z) = z j_J(z), \quad v_J(z) = z n_J(z), \quad w_J^{(+)}(z) = e^{i\pi(J+1)}[v_J(z) - i u_J(z)], \\ w_J^{(-)}(z) = w_J^{(+)}(-z) = e^{i\pi J} w_J^{(+)}(z)^*, \end{aligned} \tag{13}$$

where the star indicates complex conjugation and the prime in (11) and (12) indicates differentiation with respect to the argument.

The representations (8) and (10) of Q_{ext} are identical. The connection is established via

$$a_n = \frac{1}{2}\left(1 - \Re S_e^n\right), \quad b_n = \frac{1}{2}\left(1 - \Re S_m^n\right). \tag{14}$$

While (8) and (10) are equivalent, Newton's notation in (11) and (12) emphasizes the physical meaning of the input quantities in Q_{ext} as the two types of radiation, namely electric and magnetic multi-pole radiation [1]. This is convenient, in particular for a classification of the features observed in Q_{ext} as a function of x. Therefore, for the rest of this paper, we will adhere to Newton's notation [22]. The expansions (8) and (10) are known as partial-wave expansions, since each term in the expansion corresponds to a specific scattering mode. This is most prominently exhibited by (11) and (12), where S_e^J is the amplitude for scattering into the electric partial wave represented by the transverse vector spherical harmonic $Y_{JM}^{(e)}$ and S_m^J is the amplitude for scattering into the magnetic partial wave represented by the transverse vector spherical harmonic $Y_{JM}^{(m)}$, where the indices e and m stand for electric and magnetic, respectively, and M, an integer, ranges from $-J$ to J in steps of 1.

At this point we have assembled all the tools necessary to plot the extinction efficiency Q_{ext} as a function of x. The red curve in Fig. 1 shows Q_{ext}, calculated according to (10), in the interval $0 < x < 17$ for $n = 1.48$, the approximate index of refraction of PMMA in the transition region between the optical and the near infrared [21]. We see that Q_{ext} exhibits the following three distinctive features.

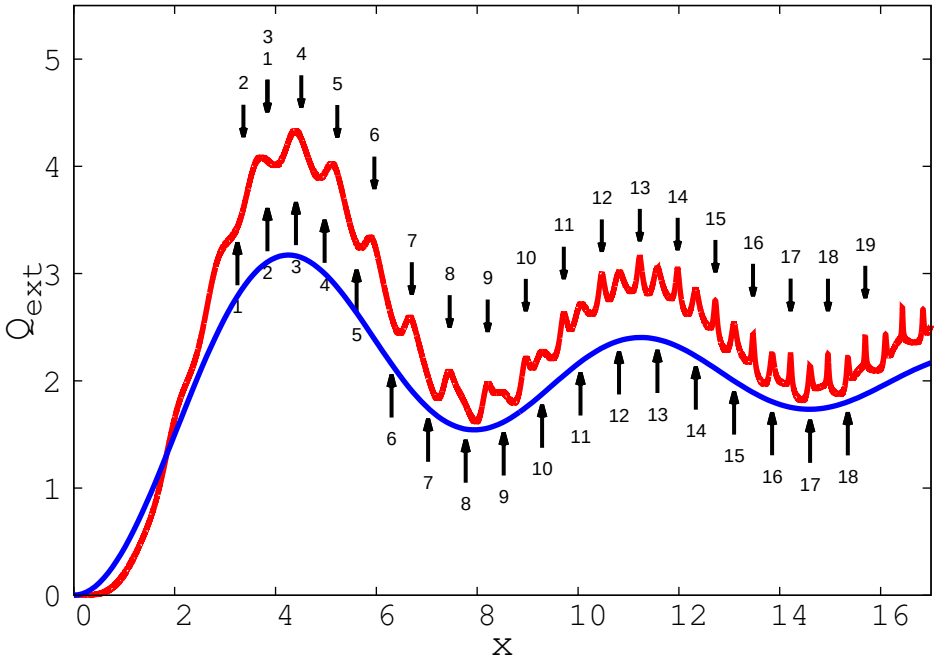

FIG. 1: (Color online) Red, solid line: Extinction efficiency $Q_{\rm ext}$ as a function of size parameter x for $n = 1.48$. A ripple structure is observed, superimposed on a wavy background. As x increases, the ripples become sharper. Each ripple is associated with a partial-wave resonance in either the electric (S_e^J) or magnetic (S_m^J) S-matrix elements. Downward arrows point to the magnetic resonances while upward arrows point to the electric resonances. The J classification of magnetic and electric ripples is shown above and below the tails of the respective arrows. The magnetic peaks $J = 1$ and $J = 3$ are nearly degenerate and also nearly degenerate with the electric $J = 2$ peak. Blue, solid line: Analytical van de Hulst approximation of Q_{ext} according to (16).

1. **Long-range oscillations:** This feature is explained by an interference effect. The phase lag between the central ray passing through a sphere of refractive index n compared to the same ray in the absence of the refracting sphere is

$$\rho = 2x(n-1). \tag{15}$$

This phase lag may be used to derive an approximate analytical expression for the long-range oscillations in $Q_{\rm ext}(x)$, first obtained and published by van de Hulst [4],

$$Q_{\rm ext}(x) = 2 - \frac{4}{\rho}\sin(\rho) + \frac{4}{\rho^2}[1-\cos(\rho)]. \tag{16}$$

It is shown as the blue solid line in Fig. 1. The fit is not perfect, but captures the frequency of the long-range oscillations very well. In particular, the fit is convincing

enough to indicate that the basic physical origin for the long-range oscillations as an interference effect is properly captured.

2. **Ripples:** This feature, a fine structure of peaks superimposed on the long-range oscillations in $Q_{\rm ext}$, is due to partial-wave resonances in the S-matrix elements (S_e^J) and (S_m^J) defined in (11) and (12), respectively [7, 8]. The resonances are called ripples in [4]. Since the ripples form the basis for our technique of extracting the radius and index of refraction of dielectric spheres from synchrotron FTIR spectra, we will discuss the ripples in more detail below.

3. **Extinction Paradox:** As shown in Fig. 1, $Q_{\rm ext}$ oscillates around a value in the vicinity of 2, about twice the classically expected $Q_{\rm ext} = 1$. This is known as the extinction paradox (see, e.g., [24]), resulting from a combination of scattering and diffraction, widely discussed and explained in the literature (see, e.g., [4, 22, 24]).

The resonance structures in $Q_{\rm ext}(x)$, i.e., the ripples (see Fig. 1), are due to the complex zeros of the denominators of the S-matrix elements S_e^J and S_m^J in (11) and (12), respectively, which correspond to poles of the S-matrix elements in the complex x plane. In general, if the S-matix poles are far from the real x axis, i.e., they have a large imaginary part, the corresponding resonances are wide; if the poles are close to the real x axis (small imaginary part), the corresponding resonances are sharp [22]. Apparently, as shown in Fig. 1, in the case of Mie scattering, the resonances, i.e., the ripples, are getting sharper with increasing x. Electromagnetic waves with fixed J are also known as partial waves [22]. Therefore, the ripples in Fig. 1 are partial-wave resonances [7, 8, 22].

For each J there is an infinite sequence of partial-wave resonances that occur at positions denoted by $x_{J,p}$, $p = 1, 2, \ldots$, ordered such that $x_{J,p+1} > x_{J,p}$. This is illustrated in Fig. 2, which shows the S-matrix elements $S_e^{J=13}$ and $S_m^{J=13}$ as a function of x for $n = 1.48$.

In order to classify the ripple (resonance) structure in $Q_{\rm ext}$, we introduce the notation $(J, M; e)$ und $(J, M; m)$ to denote the electromagnetic modes corresponding to electric and magnetic 2^J-pole radiation, respectively. For instance, the mode $(1, M; e)$ corresponds to electric dipole radiation [1] where M may assume the values $-1, 0, +1$. For a spherical scatterer the resonance positions depend only on J; they are degenerate in M.

According to [7] the spacings between resonances of a given mode do not depend on the

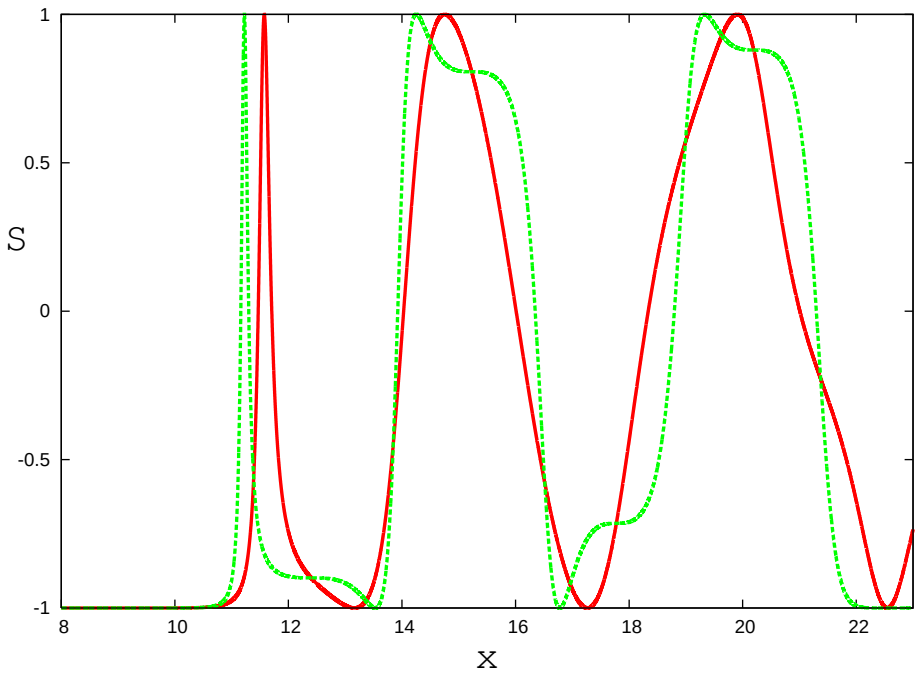

FIG. 2: (Color online) S-matrix elements $S_e^{J=13}$ (red, solid line) and $S_m^{J=13}$ (green, dashed line) as a function of size parameter x for $n = 1.48$. Both S-matrix elements exhibit an infinite series of resonances; the first three of them are shown in the figure. The first resonance, in both the electric and magnetic S-matrix elements, is sharp, followed by broader resonances for larger x. The first (sharp) magnetic peak occurs at $x = 11.2245$; the first (sharp) electric peak occurs at $x = 11.5750$.

nature of this mode (electric or magnetic) and are given approximately by [7]

$$\Delta x(n) = \frac{\arctan\left[(n^2-1)^{1/2}\right]}{(n^2-1)^{1/2}}. \tag{17}$$

This shows that the spacing between resonances is approximately independent of x and depends only on the refractive index n. Therefore, we may use the spacings between experimentally observed ripples to determine the index of refraction and its dependence on the wavelength (dispersion).

Formula (17) is reasonably accurate. For $n = 1.48$, e.g., and in the wavenumber range of interest in this paper ($3000\,\mathrm{cm}^{-1}$,..., $8000\,\mathrm{cm}^{-1}$), (17) is accurate to within about 2%. In addition, for $n = 1.48$ and J in the vicinity of 13, it is even accidentally exact. While a 2% accuracy is sufficient for rough estimates, a precision determination of the index of refraction from synchrotron FTIR spectra requires better accuracy. In this case we need to resort to the exact computation of Δx via (10), (11), and (12).

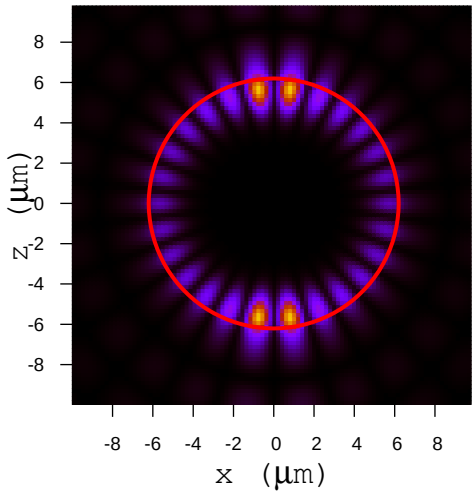

FIG. 3: (Color online) Heat map of the absolute square of the electric field of the $J = 13$, $M = 0$ magnetic mode $(J = 13, M = 0; m)$ at $x = 11.224$ in the x-z equatorial plane of a dielectric sphere with radius $R = 6.2\,\mu$m and index of refraction $n = 1.48$. The brighter the color, the larger the magnitude of the electric field. Also shown (red solid line) is the intersection of the surface of the sphere and the equatorial x-z plane.

From (17) we obtain

$$\frac{d\Delta x(n)}{dn} = -\left[\frac{n}{(n^2-1)^{3/2}}\right]\arctan\left[(n^2-1)^{1/2}\right] + \frac{1}{n(n^2-1)}. \tag{18}$$

At $n = 1.48$ we obtain $d\Delta x/dn = -0.38$. This shows that the index of refraction n reacts reasonably sensitively to changes in Δx, a prerequisite for using ripple spacings for determining the index of refraction.

In order to illustrate the mode structures of the resonances in Fig. 1, we show in Fig. 3, as an example, the electric-field distribution of the $J = 13$, $M = 0$ magnetic mode $(J = 13, M = 0; m)$ that occurs at $x = 11.224$ in Fig. 1. Shown is the absolute square, $|\vec{E}|^2 = \vec{E}\cdot\vec{E}^*$ (the star denotes complex conjugation), of the electric field of the mode in the x-z equatorial plane of a dielectric sphere with radius $R = 6.2\,\mu$m and index of refraction $n = 1.48$. We see that in analogy to a whispering-gallery mode in acoustics [25] or dielectric microresonators [26], the electric field strength is guided along the surface of the sphere and is maximal just

inside of the sphere, very close to the sphere's surface. Since total internal reflection accounts for the confinement of this wave, the quality factor Q for these modes is extraordinarily large. Counting the maxima of the field in Fig. 3, we obtain 26, which is $2J$. This is consistent, since in Fig. 3 we plot the absolute square of $\vec{E}$, which produces two maxima per wavelength.

As shown in Fig. 1, the resonances corresponding to the magnetic modes are about a factor 2 sharper than the resonances corresponding to electric modes. Therefore, in the following, we will concentrate on analyzing the magnetic modes exclusively. The sharpness of the magnetic resonances also gives us better resolution, which helps greatly in assigning the correct mode numbers to the ripples in FTIR spectra.

III. EXPERIMENT

To test the theory and in order to find out whether synchrotron-based FTIR spectroscopy is powerful enough and has enough resolution to exhibit ripples in the extinction spectrum, we measured the extinction spectrum of a polymethyl methacrylate (PMMA) microsphere taken from a sample of PMMA microspheres, purchased from MicrospheresNanospheres (Corpuscular Inc, NY). The sample was labeled by the manufacturer as consisting of plain PMMA spheres with an average diameter of $5.5\,\mu$m. The spread of diameters in the sample was not given. From this sample we selected a sphere at random and used it in our measurements without any modifications.

In order to obtain a high-quality spectrum for this sphere, we used synchrotron radiation provided by the MAX III synchrotron facility in Lund, Sweden. The $Q_{\rm ext}$ spectrum of the sphere was recorded with a resolution of $2\,{\rm cm}^{-1}$ in the wavenumber range from $650\,{\rm cm}^{-1}$ to $8000\,{\rm cm}^{-1}$ as an average consisting of 256 individual scans with a Bruker Hyperion 3000 IR microscope (Bruker Optik, Germany), coupled with an FTIR spectrometer (Bruker IFS66V), equipped with a liquid-nitrogen-cooled single-element mercury cadmium telluride (MCT) $100\,\mu{\rm m}\times 100\,\mu{\rm m}$ detector. We used a $15\times$ objective with an aperture size of $10\,\mu{\rm m}\times 10\,\mu{\rm m}$. As a substrate, 3 mm-thick ZnSe spectrophotometric optical slides were used, and a clean ZnSe plate was used as a reference.

The raw experimental $A(\tilde{\nu})$ spectrum was converted to $Q_{\rm ext}(\tilde{\nu})$ via (7). Since we are interested in the *structure* of the experimental $Q_{\rm ext}(\tilde{\nu})$ spectrum, not the absolute magnitude, no attempt was made to obtain an accurate value for the factor $f = G/g$ in (7). Instead we

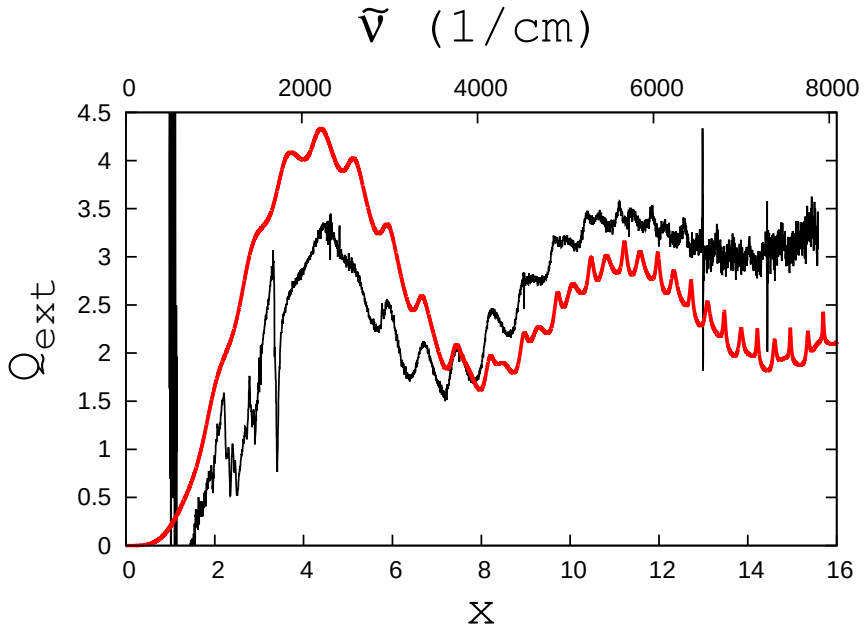

FIG. 4: (Color online) $Q_{\rm ext}$ for the experimentally measured sphere versus the size parameter x (bottom scale). The top scale shows the wavenumber $\tilde{\nu}$ in 1/cm. The conversion between x and $\tilde{\nu}$ is accomplished by assuming a sphere radius of $3.15\,\mu$m. Black, solid line: Experimental result of our synchrotron infrared absorption measurements. Red, solid line: Theoretical extinction efficiency imported from Fig. 1. The experimental extinction curve shows both wiggles (long-range oscillations) and ripples (sharp partial-wave resonances). The features in the experimental extinction spectrum are seen to line up with corresponding features in the theoretical spectrum.

use this factor as a scale factor to shift the experimental $Q_{\rm ext}(\tilde{\nu})$ spectrum into the vicinity of the theoretical $Q_{\rm ext}(\tilde{\nu})$ spectrum for convenient comparison. Since we are working with a sphere, which nominally has a diameter of $5.5\,\mu$m, and since our aperture is $10\,\mu\text{m}\times 10\,\mu$m, a good estimate for f is $f = 10\,\mu\text{m}\times 10\,\mu\text{m}/[\pi\times(2.75\,\mu\text{m})]^2 = 4.2$. We chose $f = 5$ for a good visual presentation of the data.

Although we already see ripples in the raw spectrum, the raw $Q_{\rm ext}(\tilde{\nu})$ data are noisy and many of the ripples are hidden in the noise. To bring them out, we performed a running average on the raw data according to

$$\bar{Q}_{\rm ext}(\tilde{\nu}) = \frac{1}{21}\sum_{j=-10}^{10} Q_{\rm ext}(\tilde{\nu}+js) \tag{19}$$

where $s = 0.964\,\text{cm}^{-1}$ is the wavenumber step-size in our experiments. The resulting averaged experimental spectrum with $f = 5$ is shown as the black solid line in Fig. 4. Ripples in

the $\bar{Q}_{\rm ext}(\tilde{\nu})$ spectrum are now clearly visible. Also shown is the theoretical $Q_{\rm ext}(\tilde{\nu})$ spectrum (red, solid line) that we imported into Fig. 4 directly from Fig. 1 without any modifications. We see that both wiggles and ripples in the experimental spectrum line up very well with the corresponding structures in the theoretical spectrum. No agreement between the experimental $\bar{Q}_{\rm ext}(\tilde{\nu})$ spectrum and the corresponding theoretical spectrum is expected for $\tilde{\nu} < 3000\,{\rm cm}^{-1}$, since PMMA absorbs strongly in this wavenumber region. Therefore, we focus in this paper on the wavenumber region $\tilde{\nu} > 3000\,{\rm cm}^{-1}$.

Table I lists the positions of 14 sharp, consecutive ripples, extracted from the averaged experimental spectrum in Fig. 4. These ripples correspond to $p = 1$ magnetic modes, whose angular momenta J were assigned unambiguously (see Table I). The first resonance listed in Table I ($J = 6$) is the first resonance to the right of the absorption region.

TABLE I: Locations $\tilde{\nu}$ (in ${\rm cm}^{-1}$) of experimental $p = 1$ magnetic Mie resonances extracted from the experimental FTIR spectrum (black, solid line in Fig. 4) for the measured PMMA sphere. The error in the listed wavenumbers, due to uncertainty in determining the peak locations, is approximately $\pm 5\,{\rm cm}^{-1}$.

J	$\tilde{\nu}$	J	$\tilde{\nu}$	J	$\tilde{\nu}$
6	3028	11	4950	16	6822
7	3450	12	5338	17	7204
8	3827	13	5703	18	7581
9	4233	14	6078	19	7962
10	4589	15	6448		

IV. PMMA INDEX OF REFRACTION: KNOWN RESULTS

Experimental data for the PMMA refractive index in the mid to far IR regions are not available. Therefore, based on data available in the optical and near IR regime, we need to extrapolate. Two extrapolation methods are available: Cauchy and Sellmeier.

Cauchy's formula [18], first published in the 1830s [19], is given explicitly by

$$n(\lambda) = B + \frac{C}{\lambda^2} + \frac{D}{\lambda^4} + \cdots , \tag{20}$$

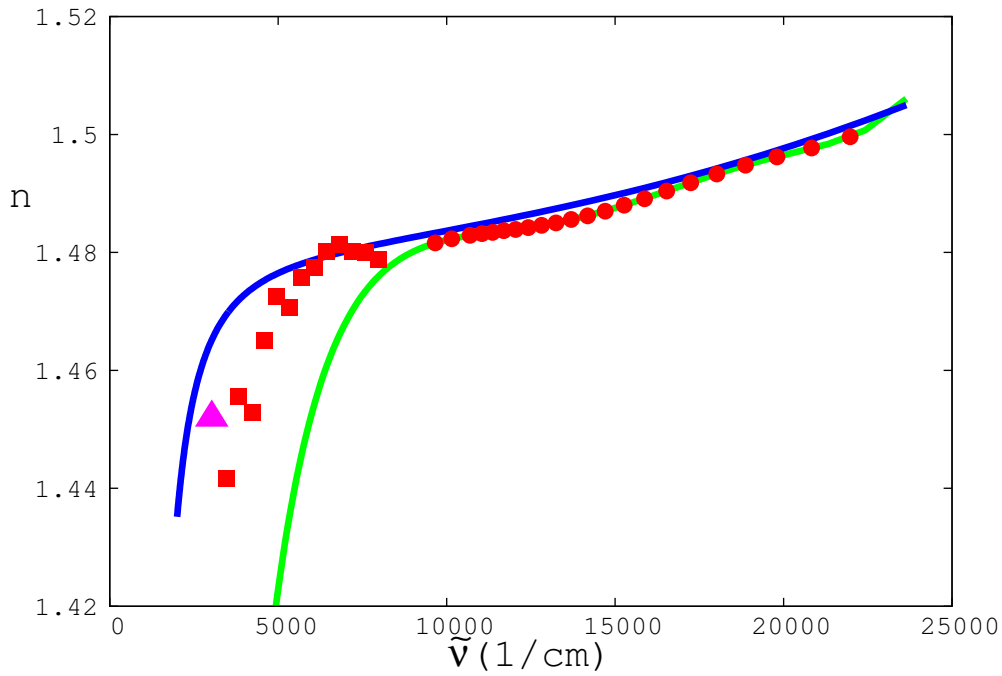

FIG. 5: (Color online) PMMA index of refraction vs. wavenumber. Red plot symbols: Experimental data according to [21]. Green line: Fit of the experimental data points with an extended Cauchy formula [21]. Blue line: Three-term Sellmeier fit of the PMMA index of refraction according to [27]. Red, filled squares: Index of refraction as a function of wavenumber extracted from our experimental FTIR synchrotron data. Magenta, filled triangle: Data point for $J = 6$. As an outlier it is characterized by a different plot symbol.

where B, C, D, ... are fit parameters and λ is the vacuum wavelength of the incident light. An extended Cauchy formula, keeping terms up to 8th order in (20), was fitted by the authors of [21]. The result is shown as the green line in Fig. 5. Apparently, in the optical and near-infrared regimes the fit is excellent. However, Cauchy's formula is known to be unreliable outside the fit region and should not be used to extrapolate too far into the mid- and far-infrared regions.

Sellmeier's formula [18], first published in 1871 [20], is explicitly given by

$$n(\lambda) = \left[1 + \sum_j \frac{A_j \lambda^2}{\lambda^2 - B_j^2}\right]^{1/2} . \tag{21}$$

A three-term Sellmeier formula for PMMA is fitted in [27]. These authors quote: $A_1 = 0.4963$, $B_1 = 71.80$nm, $A_2 = 0.6965$, $B_2 = 117.4$nm, and $A_3 = 0.3223$, $B_3 = 9237$nm. The result is shown as the blue line in Fig. 5. It is known that, compared with Cauchy's

formula, Sellmeier's formula is considerably more reliable for extrapolation into the mid- and far-infrared regions. This is corroborated by the following argument. According to Table I, the spacing $\Delta\tilde{\nu}$ between magnetic resonances is nearly constant from $J = 13$ to $J = 19$, corresponding to wavenumbers ranging from $\tilde{\nu} = 5703\,\mathrm{cm}^{-1}$ to $\tilde{\nu} = 7962\,\mathrm{cm}^{-1}$. This indicates that, according to (17), the index of refraction of our PMMA sphere in this wavenumber range is nearly constant. This is inconsistent with the strong wavenumber dependence of the Cauchy extrapolation formula in this wavenumber range (see Fig. 5) and suggests that, as expected, the Sellmeier extrapolation formula in this spectral regime is more reliable than the Cauchy formula.

V. SPHERE RADIUS

In this section we describe several methods that are capable of determining the radius of an isolated dielectric sphere and its index of refraction from measured (FTIR) extinction data. While the methods described are applicable in general to the determination of the radius of any transparent, dielectric sphere, we will apply these methods, as a specific example, to the determination of the radius of our measured PMMA sphere.

Our first method is purely analytical and yields a rough analytical estimate of the radius R of our measured PMMA sphere. For constant R and corresponding x and $\tilde{\nu}$ intervals, Δx and $\Delta\tilde{\nu}$, respectively, (9) implies

$$\Delta x = 2\pi R \Delta\tilde{\nu}, \tag{22}$$

which may be solved for R to yield

$$R = \frac{\Delta x}{2\pi\Delta\tilde{\nu}}. \tag{23}$$

As pointed out in Sec. IV, in the wavenumber interval from $J = 13$ ($5703\,\mathrm{cm}^{-1}$) to $J = 19$ ($7962\,\mathrm{cm}^{-1}$) (see Table I for the assignment of wavenumbers to J values), the spacing $\Delta\tilde{\nu}$ between magnetic resonances is nearly constant. Since there are six spacings in this wavenumber interval, the average spacing is

$$\Delta\tilde{\nu} = (7962\,\mathrm{cm}^{-1} - 5703\,\mathrm{cm}^{-1})/6 = 377\,\mathrm{cm}^{-1}. \tag{24}$$

We also argued in Sec. IV that Sellmeier's formula is realistic in this wavenumber interval. It predicts an index of refraction of $n \approx 1.48$, for which (17) yields $\Delta x = 0.760$. Using this

value of Δx together with (24) in (23), we obtain

$$R = 3.21\,\mu\text{m}. \tag{25}$$

Instead of using the analytical formula (17) for the average spacing Δx, our second method uses the exact spacing derived from the exact peaks in $Q_{\text{ext}}(x)$. For $n = 1.48$ the magnetic $J = 13$ peak in the exact $Q_{\text{ext}}(x)$ occurs at $x = 11.2225$, while the peak at $J = 19$ occurs at $x = 15.6959$. This implies an average spacing of $(15.6959 - 11.2225)/6 = 0.746$, which, used together with (24) in (23), yields

$$R = 3.15\,\mu\text{m}. \tag{26}$$

We may also base our radius estimate on the $J = 19$ ripple itself. Starting directly with (9), we have:

$$R = \frac{x_{J=19}}{2\pi\tilde{\nu}_{J=19}} = \frac{15.70}{2\pi\,7962\,\text{cm}^{-1}} = 3.14\,\mu\text{m} \tag{27}$$

All three results, (25), (26), and (27) are consistent within about $\pm 35\,\text{nm}$.

In order to obtain a rough analytical estimate of the expected uncertainty ΔR in R, we allow an error of $\delta\Delta\tilde{\nu} = 5\,\text{cm}^{-1}$ in $\Delta\tilde{\nu}$ and an error of $\delta n = 0.002$ in n and compute ΔR according to

$$\Delta R = \left[\left(\frac{\partial R}{\partial n}\delta n\right)^2 + \left(\frac{\partial R}{\partial \Delta\tilde{\nu}}\delta\Delta\tilde{\nu}\right)^2\right]^{1/2} \tag{28}$$

$$= R\left[\left(\frac{1}{\Delta x}\frac{d\Delta x}{dn}\delta n\right)^2 + \left(\frac{\delta\Delta\tilde{\nu}}{\Delta\tilde{\nu}}\right)^2\right]^{1/2}, \tag{29}$$

where we used (23). Using the analytical expression (18) to compute $d\Delta x/dn$ and using the assumed uncertainties in n and $\Delta\tilde{\nu}$, we obtain

$$\Delta R = 0.04\,\mu\text{m}. \tag{30}$$

This is consistent with the three values obtained by our three methods above. According to (30), the relative error in R amounts to $\Delta R/R = 0.013$, which is less than 2%. Thus, while not as precise as optical methods for the determination of sphere radii [9, 10], our method using FTIR in the infrared domain is quite adequate for biophysical applications and may be improved by pushing synchrotron FTIR to its current practical limit of $\Delta\tilde{\nu} \approx 1\,\text{cm}^{-1}$.

VI. PMMA DISPERSION IN THE NEAR-INFRARED

In this section we determine the PMMA index of refraction as a function of wavenumber for our measured PMMA sphere. While we expect that this data is representative of PMMA, we should not expect that the fine details of this data are reproducible as a characteristic of PMMA itself. In fact, the precise index of refraction n of PMMA depends on the specific batch of PMMA under investigation since there are natural variations depending on the production process. Therefore, we should not expect reproducibility between different batches of PMMA, but only for optical components produced from the same batch of PMMA. In [28], e.g., PMMA provided by four different suppliers showed variations in n of about ± 0.006. As we will see below, the refractive index extracted from our synchrotron data is sensitive to these variations.

We derive the dispersion $n(\tilde{\nu})$ of our measured PMMA sphere assuming that its radius, determined according to our direct method [see (27)], is $R = 3.14\,\mu$m. In this case we may start from (9) and write

$$x_J(n_J) = 2\pi R\tilde{\nu}_J, \tag{31}$$

where $x_J(n)$ is the position of the ripple corresponding to the magnetic mode with angular momentum J and index of refraction n. For given J, the function $x_J(n)$ is known. It may, e.g., be computed by determining the position of the $p = 1$ pole of $S_m^J(x; n)$ in (12), or it may be determined graphically from wavenumber sweeps of $Q_{\text{ext}}(\tilde{\nu})$, since, although all partial waves contribute to $Q_{\text{ext}}(\tilde{\nu})$, at the position of a ripple with angular momentum J, the partial wave with mode number J will dominate. In our determination of $x_J(n)$ we used the $Q_{\text{ext}}(\tilde{\nu})$-sweep method.

Since we assume that R, $x_J(n)$, and $\tilde{\nu}_J$ are known, we may now determine the index of refraction of our PMMA sphere at $\tilde{\nu}_J$ by inverting (numerically), equation (31) according to

$$n_J = n(\tilde{\nu}_j) = x_J^{-1}(2\pi R\tilde{\nu}_J), \tag{32}$$

where x_J^{-1} is the inverse function of x_J. The result of (32) for ripples with $J = 7, \ldots, 19$, listed in Table I, is shown as the red filled squares in Fig. 5. Also shown is the result for the ripple with $J = 6$ (magenta triangle in Fig. 5). This data point is shown as a different plot symbol, since, according to Fig. 4, it sits on a wing and, in addition, represents the merger of a magnetic and an electric ripple. This may give rise to large shifts in wavenumber, which

make this point unreliable.

VII. DISCUSSION

We are not the first to use synchrotron infrared radiation for extinction measurements on PMMA spheres. Several previous measurements are reported in the literature [13–15]. However, all of these previous measurements are preformed in the infrared regime with wavenumbers $\lesssim 4000\,\mathrm{cm}^{-1}$ where strong absorption due to chemical absorption bands occurs, which obscures the ripples in the absorption spectrum. In our measurement, in a deliberate attempt to access the regime of ripples, we extended the wavenumber range to $8000\,\mathrm{cm}^{-1}$, above the chemical absorption regime, in which, for spheres with a radius of $R \lesssim 10\,\mu\mathrm{m}$, the ripples are fully formed. We conducted FTIR spectroscopy on PMMA spheres as a pilot project for our ultimate goal, FTIR spectroscopy on cells and other microscopic, quasi-spherical biological structures, such as plant pollen. From our experiments with PMMA spheres we learn that FTIR spectroscopy is a powerful tool that, under ideal conditions, such as presented by PMMA spheres, is capable to determine radii and the dispersion of the index of refraction. In order to accomplish this, however, the conventional FTIR range, which typically ranges up to $4000\,\mathrm{cm}^{-1}$, needs to be extended to at least $8000\,\mathrm{cm}^{-1}$, as done in our experiments, in order to access the wavenumber regime above $4000\,\mathrm{cm}^{-1}$ in which most organic materials, including PMMA, do not show chemical absorption bands. Including this wavenumber regime in spectroscopic sweeps, as shown here for PMMA, provides valuable physical information on the specimen under investigation.

If we would like to extract information from the ripple structure of a scatterer, it is important to work with *isolated* scatterers. For instance, in his Ph.D. thesis [14], Bassan shows the FTIR spectrum of a PMMA sphere that is in contact with and surrounded by at least four neighboring PMMA spheres. Although only the central sphere is illuminated, the resulting spectrum is smooth and does not show any ripples. This effect is understandable, since, as shown in Sec. II, the ripples are due to whispering gallery modes, and touching spheres spoil the whispering gallery-mode structure, characteristic for single, isolated spheres. This is so, since touching spheres are strongly coupled via tunneling, which results in Q-spoiling, an effect well-known in the field of microdisk lasers [29].

Because we are scattering from a sphere, the ripples (resonances) are degenerate in M.

In this case it is enough to specify (J, e) or (J, m) to classify individual ripples. This is what, implicitly, we did in Fig. 1, where, in addition to classifying ripples according to whether they are electric or magnetic, we use only one additional mode number, J, to characterize each ripple. In case the sphere is slightly deformed, has a rough surface, or has a non-spherical, inhomogeneous index of refraction, the single peaks in Q_{ext} will split into multiplets. In this case a different classification scheme has to be constructed. If the deformation is too large, it is well known from the field of quantum chaos [30] that the resulting resonance structure is chaotic, and a straightforward classification scheme may be impossible in principle [31].

When irradiated with synchrotron light, the sphere itself turns into a radiation source and emits electromagnetic radiation. For wave numbers corresponding to ripples, either the electric or magnetic 2^J-pole radiation is especially strong and causes a peak in Q_{ext}. This is so, since on resonance a larger amount of light than in the off-resonance case is removed from the incident beam and re-radiated, essentially isotropically (especially for large J), in all directions. In case the wavelength is small and therefore the wave number is large, modes with relatively large J are excited as demonstrated in Fig. 3, where the electric field distribution of the magnetic $J = 13$ mode is shown. $J = 13$ corresponds to $2^{13} = 8192$-pole radiation. It is surprising that such high-order multipole radiation can be resolved in our FTIR synchrotron experiments.

The electromagnetic field in Fig. 3 is computed and plotted using the formulas for the electric and magnetic fields in [22]. However, we noticed a problem: The factors κ and k in the denominators of equations (2.122), (2.123) and (2.124), (2.125) in [22] are inconsistent and lead to electric and magnetic field modes that do not satisfy the boundary conditions. Deleting these factors of κ and k yields consistent expressions for the electric and magnetic fields, which we then used to plot Fig. 3.

A synchrotron beam is very intense and the question of heating the sample under investigation may arise. Although a synchrotron beam is more intense than a beam generated by, for instance, a *Globar* infrared source [32], the intensity is still low enough that heating of the sample can be completely neglected. This is corroborated by the photon flux per unit wavenumber, which is very small.

Small spheres, such as the sphere measured in our FTIR synchrotron experiments, are useful for absolute calibrations. This is so, since for small spheres wiggles and ripples have a one-to-one correspondence with theoretical simulations of Q_{ext}. Since for small spheres even

the large-wavelength part of the spectrum is essentially undistorted by chemical absorption, the J classification of magnetic and electric modes can be accomplished unambiguously. This helps greatly in determining both the radius of a sphere and the dispersion of the index of refraction. Of course, a 5-micron sphere, e.g., covers only half the x range of a 10-micron sphere. However, there is an upside: Precisely because only half the x range is covered for the same wavenumber range, the extinction spectrum of a 5-micron sphere has effectively twice the resolution than the extinction spectrum of a 10-micron sphere. This fact considerably facilitates the mode-number assignment of the spectra of small spheres. On the downside, the spectra of small spheres do not quite reach the high-x regions where the ripples become sharp.

VIII. SUMMARY AND CONCLUSIONS

In this paper we showed that the ripple structure in synchrotron FTIR extinction spectra is capable of determining the radius of a dielectric sphere with great accuracy. In addition, we showed that the ripple structure allows us to extract the frequency-dependent index of refraction of PMMA in a wavenumber regime where it has not previously been measured. Both the determination of an unknown sphere radius and the determination of the dispersion of the index of refraction are applicable to any transparent material that can be shaped into spheres. Thus, FTIR is shown to be a capable method for determining the index of refraction in the infrared regime, needed in biophysical FTIR spectroscopy, but not generally available by other means.

IX. ACKNOWLEDGEMENTS

We would like to thank the staff of the MAX III synchrotron in Lund, Sweden, in particular Anders Engdahl, for valuable assistance. Financial support by the Norwegian Science Council under grant number 216687, "Hyperspectral imaging in biophysics and energy physics", is gratefully acknowledged.

---

[1] J. D. Jackson, *Classical Electrodynamics*, second edition (John Wiley & Sons, Inc., 1975).

[2] G. Mie, "Beiträge zur Optik trüber Medien, speziell kolloidaler Metallösungen," Ann. Phys. (Leipzig) **25**, 377-452 (1908).

[3] P. Debeye, "Der Lichtdruck auf Kugeln von beliebigem Material," Ann. Phys. (Leipz.) **30**, 57-136 (1909).

[4] H. C. van de Hulst, *Light Scattering by Small Particles* (Dover, 1981).

[5] C. Hurd (editor), "The IBM 701 Thirtieth Anniversary – IBM Enters the Computing Field," Annals of the History of Computing, Vol. 5 (No. 2) (1983).

[6] R. B. Penndorf, "New Tables of Total Mie Scattering Coefficients for Spherical Particles of Real Refractive Indexes ($1.33 \leq n \leq 1.50$)," J. Opt. Soc. Am. **47**, 1010-1015 (1957).

[7] P. Chýlek, "Partial-wave resonances and the ripple structure in the Mie normalized extinction cross section," J. Opt. Soc. Am., **66**, 285-287 (1976).

[8] P. Chýlek, J. T. Kiehl, and M. K. W. Ko, "Narrow resonance structure in the Mie scattering characteristics," Appl. Optics **17**, 3019-3021 (1978).

[9] A. Ashkin and J. M. Dziedzic, "Observation of Resonances in the Radiation Pressure on Dielectric Spheres," Phys. Rev. Lett. **38**, 1351-1354 (1977).

[10] P. Chýlek, J. T. Kiehl, and M. K. W. Ko, "Optical levitation and partial-wave resonances," Phys. Rev. **18**, 2229-2233 (1978).

[11] E. J. McCartney, *Optics of the atmosphere: Scattering by molecules and particles* (John Wiley and Sons, Inc., 1976).

[12] G. Bosma, Ch. Pathmamanoharan, E. H. A. de Hoog, W. K. Kegel, A. van Blaaderen, and H. N. W. Lekkerkerker, "Preparation of Monodisperse, Fluorescent PMMALatex Colloids by Dispersion Polymerization," Journal of Colloid and Interface Science **245**, 292-300 (2002).

[13] P. Bassan, H. J. Byrne, F. Bonnier, J. Lee, P. Dumas, and P. Gardner, "Resonant Mie scattering in infrared spectroscopy of biological materials–understanding the 'dispersion artefact'," Analyst. **134**, 1586-1593 (2009).

[14] P. Bassan, "Light scattering during infrared spectroscopic measurements of biomedical samples," Ph.D. thesis (2011), unpublished.

[15] T. van Dijk, D. Mayerich, P. S. Carney, and R. Bhargava, "Recovery of Absorption Spectra from Fourier Transform Infrared (FT-IR) Microspectroscopic Measurements of Intact Spheres," Applied Spectroscopy **67**, 546-552 (2013).

[16] M. C. McCann, M. Hammouri, R. Wilson, P. Belton, and K. Roberts, "Fourier-tranform

infrared microspectroscopy is a new way to look at plant-cell walls," Plant Physiology **100**, 1940-1947 (1992).

[17] P. Lasch, A. Pacifico, and M. Diem, "Spatially resolved IR microspectroscopy of single cells," Biopolymers **67**, 335-338 (2002).

[18] M. Born, *Optik*, third edition (Springer, 1972).

[19] L. Cauchy, Bull. des sc. math. **14**, 9 (1830); "Sur la dispersion de la limière," Nouv. exerc. de math. (1836).

[20] W. Sellmeier, "Zur Erklärung der abnormen Farbenfolge im Spektrum einiger Substanzen," Ann. Phys. Chem. **219**, 272-282 (1871).

[21] S. N. Kasarova, N. G. Sultanova, Ch. D. Ivanov, and I. D. Nikolov, "Analysis of the dispersion of optical plastic materials," Optical Materials **29**, 1481-1490 (2007).

[22] R. G. Newton, *Scattering Theory of Waves and Particles* (McGraw-Hill, 1966).

[23] *Handbook of Mathematical Functions*, edited by M. Abramowitz and I. A. Stegun (National Bureau of Standards, 1964).

[24] M. J. Berg, C. M. Sorensen, A. Chakrabarti, "A new explanation of the extinction paradox," Journal of Quantitative Spectroscopy & Radiative Transfer **112**, 1170-1181 (2011).

[25] J. W. S. Rayleigh, *Theory of Sound*, vol. II, 1st edition (MacMillan, 1878); (Dover, 1945).

[26] A. Chiasera, Y. Dumeige, P. Féron, M. Ferrari, Y. Jestin, G. Nunzi Conti, S. Pelli, S. Soria, and G. C. Righini, "Spherical whispering-gallery-mode microresonators," Laser and Phot. Rev. **4**, 457-482 (2010).

[27] T. Ishigure, E. Nihei, and Y. Koike, "Optimum refractive-index profile of the graded-index polymer optical fiber, toward gigabit data links," Applied Optics **35**, 2048-2053 (1996).

[28] F. Languy, K. Fleury, C. Lenaerts, J. Loicq, D. Regaert, T. Thibert, and S. Habraken, "Flat Fresnel doublets made of PMMA and PC: combining low cost production and very high concentration ratio for CPV," Optics Express **19**, A280-A294 (2011).

[29] J. U. Nöckel, A. D. Stone, and R. K. Chang, "Q spoiling and directionality in deformed ring cavities," Opt. Lett. **19**, 1693-1695 (1994).

[30] H.-J. Stöckmann, *Quantu Chaos: An Introduction* (Cambridge Univ. Press, 1999).

[31] M. C. Gutzwiller, *Chaos in Classical and Quantum Mechanics* (Springer, 1990).

[32] L. G. Bonner, "A New Type Globar Support for Infrared Spectrometry," Rev. Sci. Instruments **8**, 264-265 (1937).